Accessing self-diffusion on nanosecond time and nanometre length scales with minute kinetic resolution

Christian Beck, Felix Roosen-Runge, Marco Grimaldo, Dominik Zeller, Judith Peters, Frank Schreiber, Tilo Seydel

To cite this version:

Christian Beck, Felix Roosen-Runge, Marco Grimaldo, Dominik Zeller, Judith Peters, et al.. Accessing self-diffusion on nanosecond time and nanometre length scales with minute kinetic resolution. Journal of Applied Crystallography, 2024, 57 (4), 10.1107/S1600576724003820 . hal-04611324

Accessing Self-Diffusion on Nanosecond Time and Nanometer Length Scales with Minute Kinetic Resolution

Christian Beck[1,2], Felix Roosen-Runge[3,4], Marco Grimaldo[1,2], Dominik Zeller[2,5], Judith Peters[2,5,6], Frank Schreiber[1], and Tilo Seydel[2]

[1]Institut für Angewandte Physik, Universität Tübingen, Auf der Morgenstelle 10, 72076 Tübingen, Germany
[2]Institut Max von Laue - Paul Langevin, 71 avenue des Martyrs, 38042 Grenoble, France
[3]Division of Physical Chemistry, Lund University, Naturvetarvägen 14, 22100 Lund, Sweden
[4]Department of Biomedical Science, Biofilms-Research Center for Biointerfaces, Malmö University, 205 06 Malmö, Sweden
[5]Univ. Grenoble Alpes, CNRS, LiPhy, Grenoble, France
[6]Institut Universitaire de France
Email: christian.beck@uni-tuebingen.de; felix.roosen-runge@mau.se; seydel@ill.eu

Abstract

Neutron spectroscopy uniquely and non-destructively accesses diffusive dynamics in soft and biological matter, including for instance proteins in hydrated powders or in solution, and more generally dynamic properties of condensed matter on the molecular level. Given the limited neutron flux resulting in long counting times, it is important to optimize data acquisition for the specific question, in particular for time resolved (kinetic) studies. The required acquisition time was recently significantly reduced by measurements of discrete energy transfers rather than quasi-continuous neutron scattering spectra on neutron backscattering spectrometers. Besides the reduction of acquisition times, smaller amounts of samples can be measured with better statistics, and most importantly, kinetically changing samples, such as aggregating or crystallizing samples, can be followed. However, given the small number of discrete energy transfers probed in this mode, established analysis frameworks for full spectra can break down. Here, we present new approaches to analyze measurements of diffusive dynamics recorded within fixed windows in energy transfer, and compare them to the analysis of full spectra. We test the new approaches by both modeled scattering functions, and a comparative analysis of fixed energy window data and full spectra on well-understood reference samples. Our new approach can be employed successfully for kinetic studies of the dynamics focusing on the short time apparent center-of-mass diffusion.

1 Introduction

To understand kinetic processes in soft and biological matter evolving on time scales from minutes to hours, such as protein aggregation and protein crystallization, suitable experimental methods have to be developed.[1–6] In order to obtain a comprehensive picture, the structural evolution is not sufficient, but these methods have to include the ability to detect diffusive dynamics on nanosecond time and nanometer length scales commensurate with protein dynamics inside living cells and with protein folding dynamics.[7] The successful development of these methods is crucial to address challenges such as the combat of protein aggregation diseases.[8–10] Neutron spectroscopy can access essential experimental observables for this endeavour, such as self-diffusion on the molecular level, without the need for specific labels[11] and is one of the few techniques along with XPCS[12] which provides length and timescale information. However, neutron spectroscopy is a fundamentally signal-limited technique due to physical constraints imposed on the neutron source brightness.

Neutron spectroscopy typically measures the dynamic structure factor $S(q,\omega)$ depending on the scattering vector q (i.e., momentum transfer $\hbar q$ related to the scattering angle) and the energy transfer $\hbar\omega$. $S(q,\omega)$ represents the Fourier transform of the van Hove correlation function $G(r,t)$ depending on space r and time t.[13] The observable timescales are given by the spectrometer resolution function and maximum energy transfer.

Cold neutron backscattering spectroscopy (NBS) achieves a very high energy resolution of typically better than $1\,\mu\text{eV}$ full width at half maximum (FWHM) for $\hbar q$ up to $q \approx 2\,\text{Å}^{-1}$ by employing Bragg reflections in exact backscattering from both monochromator and analyzer single crystals. The requirement of backscattering prohibits any change of the crystal Bragg angle for spectral recordings. Therefore, mechanical Doppler drives carrying the monochromator crystal constitute the presently most common approach to change the incident neutron energy by a Bragg reflection in a moving reference frame (Figure 1)[14–17] and are employed in current NBS instruments, such as IN16B[16] at the ILL, EMU at ANSTO,[17] HFBS at NIST,[15] or SPHERES at MLZ.[18] Their maximum speed is $v_{\text{max}} \approx 4.5\,\text{m/s}$, limited by the corresponding acceleration and the monochromator mass $\approx$ 1 kg. For comparison the speed of cold neutrons is $\approx$ 630 m/s at 2 meV energy, and thus, the Doppler effect allows to shift the neutron energy by a measurable amount. The mechanical approach is owed to the large neutron beam size ($\approx 20 \times 30\text{cm}^2$) at the monochromator position due to the focus optics built into these instruments, rendering the alternative approach of changing the monochromator lattice spacing via temperature[20,21] challenging due to the required temperature homogeneity. Among numerous applications from quantum mechanics to polymer and glass physics, NBS is particularly suited to access nanosecond diffusive dynamics.[11,22–26] This strength can for instance be exploited to measure diffusion of nanometer-size soft colloid particles such as proteins in liquid solutions, which we use as test case in this article. However, recording full spectra takes a considerable time, typically several hours, depending on experimental parameters and the sample composition, to obtain statistically meaningful data.

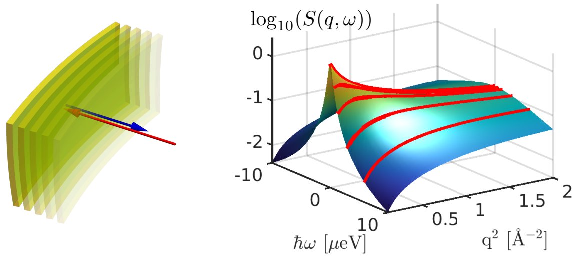

Figure 1: Left: Schematic representation of a moving monochromator crystal achieving an energy transfer in exact backscattering by a Bragg reflection in a moving reference frame, denoted Doppler monochromator. (Schematic adapted with permission from [19]). Right: Schematic of a QENS spectrum: Depending on the velocity profile (cf. Figure 2) of the Doppler monochromator, full QENS spectra (surface plot) or discrete energy transfers (red lines) can be acquired .

In this paper, we discuss strategies for more time efficiency, opening up new areas of application of NBS-based quasi-elastic neutron scattering (QENS). We propose analysis frameworks for NBS data acquired at only few selected discrete energy transfers. In addition to the obvious reduction of acquisition times and enhancement of signal, kinetically changing samples can be followed, enabling new science.

This article is organized as follows. We first explain the acquisition modes of NBS instruments with

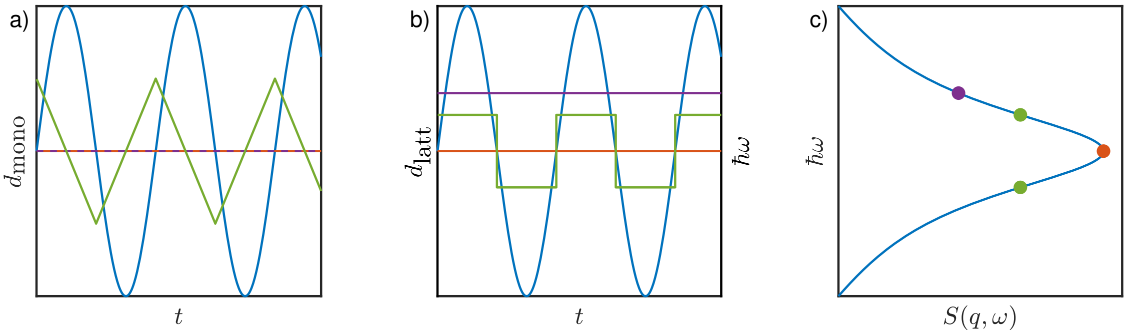

Figure 2: Different operation modes for backscattering spectrometers using a movable monochromator crystal. Blue, violet, green and orange lines represent the operation mode with a sinusoidal velocity profile, a stationary heated monochromator crystal, as well as the ones for IFWS and EFWS, respectively. The displacement profiles d_{mono} translating the reference frame as a function of time, shown in (a), translate to the effective lattice spacing d_{latt} in the laboratory rest frame (b), and, thus, to the energy transfer $\hbar\omega$ encountered by the Bragg reflected neutrons (c). Identical monochromator and analyzer crystals, with same crystal cut, are assumed. The detected scattering signal for the scenarios is shown in c) in a rotated plot to have the energy transfer aligned with the subplot b).

a Doppler monochromator. We then focus on the different contributions to the scattering signal at given energy transfers and model the incoherent scattering of protein solutions based on the description of full QENS spectra.[27] Using modeled data sets, we discuss the non-monotonous contributions to the scattering signal in Section 2. We next focus on established analysis methods (Section 3) and on the application of models established for full QENS spectra for the analysis of the data with distinct energy transfers (Section 4). Subsequently, in Section 5 we present a new approach, resulting in quantitative agreement with the analysis of full QENS spectra. Sections 6 and 7 address the applicability to powder samples and the influence of instrument resolution.

We discuss samples where the scattering signal of interest can be considered spatially incoherent due to the prevalence of the ^{1}H isotope with its large incoherent scattering cross section. The D_2O solvent scattering signal can be subtracted. Different frameworks exist for the analysis of such scattering signals.[11,28–35] Here, we analyze the ensemble-averaged single-particle self-correlation in terms of the van Hove-picture[13,36] as has been established and successfully employed in many other studies.[37–44] Being an inherently intensity-limited technique,[45] full NBS spectra with a quasi-continuous energy transfer $\hbar\|\omega\| \leqslant 30\mu\mathrm{eV}$ require typical recording times of 2 to 6h even from concentrated protein solutions, $c_p \simeq 100\,\mathrm{mg/ml}$. In addition, calibration data such as the solvent and the sample container have to be collected in comparable quality. However, the interest in kinetically changing samples has increased recently, which evolve on time scales much shorter than the above recording times. These samples can depend on external triggers or control parameters such as time,[46] temperature,[27,47–52] pressure,[53] illumination,[54,55] chemical potential,[56] or phase transitions.[5]

New technical developments for NBS, leading to higher signal-to-noise ratios up to 1:40000,[57] new neutron guides and focusing options,[58] and phase-space transformers[59,60] increasing the neutron flux on the sample position have already reduced the exposure time. Changes in the short-time dynamics of crystallizing proteins on a kinetic time-scale of 15 minutes using a floating average analysis method of full QENS spectra[46] have been reported recently. However, floating averages smear out events that occur on a kinetic time-scale lower than the exposure time for one spectrum. Thus, to obtain good time-resolved data, high intensity measurements with good statistics are needed on shorter time scales, or stroboscopic measurements can be performed.[61]

The count rate for specific energy transfers can be significantly increased by choosing a displacement profile of the monochromator which selects predominately only the specified energy transfer. The acquisition time for these discrete energy transfers is significantly shorter than the acquisition time for a full QENS spectrum with a quasi-continuous energy range and has a significantly higher count rate and therefore better statistics at the given energy transfer (see also SI). These measurements probing only a set of fixed energy transfers are called fixed window scans (FWS). A specific case is that of zero offset (see below).

Different options exist to observe fixed non-zero energy transfers, by so-called inelastic fixed window scans (IFWS): First, the energy may be offset by monochromator crystals with a lattice spacing different to the analyzers by either offsetting their temperature or by using a different crystal or a different crystal cut. In Figure 2, this first option, which is used *e.g.* on IN13,[62,63] is displayed with violet lines and points. Second, the velocity profile of the monochromator crystal can be chosen such that during a certain time the monochromatic neutrons have a constant offset $\hbar\omega$ relative to the energy set by the analyzers,[64] due to the Doppler effect.

With a Doppler monochromator,[65] acquisition can efficiently be performed at fixed transfers up to $\hbar\omega \leqslant 10\,\mu\text{eV}$[66] within exposure times $30\text{s} < t < 600\text{s}$. For these FWS, the displacement profile (Figure 2a) of the monochromator crystal is set such that it travels a major part of the available path length, typically $-75\,\text{mm} \leqslant d_{\text{mono}} \leqslant +75\,\text{mm}$, with a constant speed v, resulting in a constant effective lattice spacing d_{latt} in the moving reference frame (Figure 2b), and thus, in a constant neutron energy transfer (Figure 2c). This displacement profile corresponds to a quasi-zigzag motion, limited by the requirement of a differentiable motion obeying the technical specification of the Doppler drive (green lines and symbols in Figure 2), allowing to measure the energy transfers $\pm\hbar\|\omega\|$ while maintaining the good energy resolution of exact backscattering.

For identical monochromator and analyzer crystals with same crystal cut and temperature, $v = 0$ results in $\hbar\omega = 0$ (orange lines in Figure 2), and the measurement is denoted an elastic fixed window scan (EFWS). This specific case has been successfully employed in early works by Frick, Doster, Zaccai and others.[30,31,39,40,67] In case the sample scatters mainly incoherently, this situation is also called elastic incoherent neutron scattering (EINS). Obviously, FWS cannot provide the same amount of information as full QENS measurements, which covers a quasi-continuous energy transfer range. Nevertheless, depending on the sample and kinetics, FWS are faster and may be the preferred technique. To establish a broad range of sample parameters, proteins with different sizes, namely bovine serum albumin (BSA), polyclonal immunoglobulin (Ig), as well as myoglobulin (Myo) were investigated at different protein concentrations and temperatures in solution (Table 1). All protein solutions were prepared by dissolving a given protein mass m in a volume V of D_2O without further purification resulting in the nominal protein concentration $c_p := m/V$. The protein solutions have been investigated previously with QENS.[40,51,68–71] Moreover, hydrated protein powders were measured (Table 2). Protein powders have been prepared with final hydration levels of $h = 0.29\frac{\text{g}}{\text{g}}$ and $h = 0.32\frac{\text{g}}{\text{g}}$ for BSA in H_2O and D_2O, respectively. Given the high hydrogen ^{1}H contents in the proteins, the deuterated solvents as well as the investigated q-ranges, the signal measured is dominated by incoherent scattering. Different spectrometers allow to investigate the influence of different ranges in $\hbar q$, $\hbar\omega$, and of energy resolutions.

Table 1: Measured liquid protein solution sample conditions. All samples were measured during experiment 1-20-69[72] on IN16B at the ILL. Full QENS spectra were measured with the energy resolution $\delta E = 0.9\,\mu\text{eV}$ FWHM and 30 μeV dynamical range with a scattering vector range $0.1\text{Å}^{-1} < q < 1.8\text{Å}^{-1}$. FWS were measured with the same energy resolution and same q range at energy transfers in the interval $\hbar\omega = [0, 10]\,\mu\text{eV}$ with a step size of 0.5 μeV.

#	Temperature [K]	Sample
1	280	BSA 100mg/ml
2	280, 295, 310	BSA 500mg/ml
3	280	Myo 500 mg/ml
4	280	polyclonal Ig 500 mg/ml

Table 2: Powder sample conditions measured on the NBS instruments IN16B (beamtime 9-13-637;[73] $\delta E = 0.9\mu\text{eV}$; 0.1 $\text{Å}^{-1} < q <$1.8 Å^{-1}) and IN13 (9-13-628;[74] $\delta E = 8\mu\text{eV}$; 0.19 $\text{Å}^{-1} < q <$4.9 Å^{-1}). Both samples were measured during temperature ramps.

#	Instrument	$\hbar\omega$ [μeV]	Sample
5	IN16B	0, 1.3, 3, 6	BSA hydrated with H_2O
	IN13	3, 9	
6	IN16B	0, 1.3, 3, 6	BSA hydrated with D_2O
	IN13	3, 9	

2 Contributions to the Incoherent Scattering Signal

To describe a recorded QENS spectrum arising from diffusive dynamics, a sum of Lorentzian functions $\mathscr{L}_{\tilde{\gamma}} := \mathscr{L}(\tilde{\gamma}(q), \omega) = \gamma(q)\left(\pi(\gamma(q)^2 + \omega^2)\right)^{-1}$ with different width functions $\tilde{\gamma}(q)$ is generally employed in a suitable model function $S(q, \omega)$.[11] For our test protein solution samples (Table 1), we assume[11,75]

$$S(q, \omega) = \beta(q)\{A_0(q)\mathscr{L}(\gamma(q), \omega) + (1 - A_0(q)) \cdot \mathscr{L}(\gamma(q) + \Gamma(q), \omega)\} + \beta_{D_2O}(q)\mathscr{L}_{D_2O}(\gamma_{D_2O}(q), \omega) \quad (1)$$

$\mathscr{L}(\gamma(q), \omega)$ accounts for the apparent global center-of-mass diffusion of the proteins in solution, $\mathscr{L}(\gamma(q) + \Gamma(q), \omega)$ for the internal diffusive dynamics of the proteins convoluted with the global diffusion, and $\mathscr{L}_{D_2O}(\gamma_{D_2O}(q), \omega)$ for the solvent water signal. $\beta(q)$ and $\beta_{D_2O}(q)$ are scalars weighting the amplitudes of these contributions. $A_0(q)$ can be identified with the Elastic Incoherent Structure Factor (EISF).[76] This exemplary model can also be applied to suspensions of soft colloids.[11] The measured scattering signal $S_{\text{meas.}}(q, \omega) = \mathcal{R} \otimes S(q, \omega)$ is convoluted with the spectrometer resolution function $\mathcal{R}$ that we assume to be a zero-centered Gaussian function with the full width at half maximum $\delta E = 2\sqrt{2\ln(2)}\sigma$ with the Gaussian standard deviation σ. For the spectrometer IN16B, we assume $\delta E = 0.9\,\mu\text{eV}$.

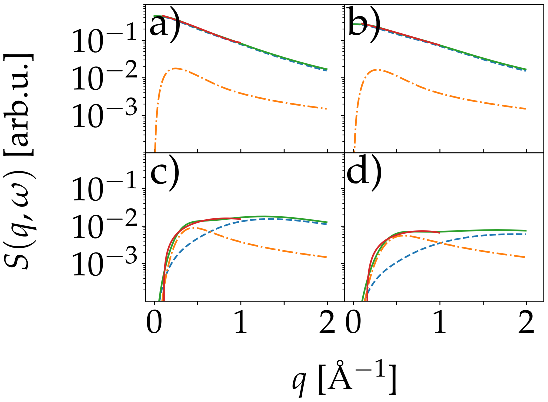

Figure 3: Modeled incoherent scattering functions of hypothetical soft colloids ($D = 2\,\text{Å}^2\mu\text{eV}$, $D_{int} = 35\,\text{Å}^2\mu\text{eV}$ and $\tau = 0.001\,\mu\text{eV}^{-1}$) in liquid suspension as a function of the momentum transfer $\hbar q$ for different energy transfers $\hbar\omega$ (a) 0 μeV, b) 0.9 μeV, c) 5 μeV, d) 10 μeV, versus q. Besides the total incoherent scattering function (solid green line), the different contributions from the apparent global diffusion (blue dashed line) as well as from the internal diffusion (orange dashed dotted line) are shown for several energy transfers. The red lines represent the fits of Equation 2. For detailed information on the modelling see main text and SI.

The q dependence of the widths $\gamma(q)$ and $\Gamma(q)$ can be described by a Fickian, $\gamma(q) = Dq^2$, and jump diffusion process $\Gamma(q) = D_{\text{int}}q^2\left(1 + D_{\text{int}}q^2\tau\right)^{-1}$ with an apparent global diffusion coefficient D, an internal diffusion coefficient D_{int} and with the residence time τ between diffusive jumps.[77] Figure 3 depicts experimental data as well as the modeled incoherent scattering depending on q for different $\hbar\omega$. The parametrization of the EISF, the assumed quantities, as well as representations of $S(q,\omega)$ versus $\hbar\omega$ for different q are shown in the SI.

We note that in solution, proteins are subject to both translational and rotational diffusion. In numerous studies, these two contributions have been shown to be combined to an apparent global diffusion as observable quantity, due to the large measured $\hbar q$,[75] which is fully accounted for by $\mathscr{L}(\gamma(q),\omega)$ in Equation 1.

Several features of the incoherent scattering function can be observed in the subplots of Figure 3. While at low energy transfers, the incoherent scattering signal decreases monotonously, it displays a maximum at higher energy transfers. In addition, the internal dynamics contribute significantly at higher energy transfers. At large q, the incoherent scattering function is dominated by the apparent global diffusion for all energy transfers $\hbar\omega$ investigated.

3 Generalized Mean Squared Displacements

EINS measurements can be approximated by a model free approach using a cumulant expansion giving access to the mean squared displacement $\langle u^2 \rangle$:[31,43,78,79]

$$\log\left(S(q,\omega=0)\right) = -\frac{1}{3}\left(b + \langle u^2 \rangle q^2 + cq^4\right). \quad (2)$$

The underlying idea is to expand the Gaussian approximation, which would only have the first two contributions, and therefore cover a larger q range. The approach in Equation 2 has the advantage of being easily implemented and model-free.

Applying Equation 2 to IFWS results in $\hbar\omega$-dependent fits such as the generalized mean squared displacement $\langle u^2 \rangle_\omega$.[80] The dependence on $\hbar\omega$ contains information on the underlying diffusive process.

This generalized MSD $\langle u^2 \rangle_\omega$ decays with increasing energy transfers investigated,

$$\langle u^2 \rangle_\omega = -\lim_{q\to 0} \frac{3}{q^2} \log\left[\frac{S(q,\omega)}{\mathscr{R}(\omega)}\right], \quad (3)$$

with $\mathscr{R}$ being the resolution function.

The energy-dependence of $\langle u^2 \rangle_\omega$ contains information on the type of the diffusive process. Importantly, $\langle u^2 \rangle_\omega$ can result in positive and negative values, which can hint at confinement effects and free or driven motions for $\hbar\omega \approx \sqrt{2}\delta E$, respectively.[80]

In Figure 4, EFWS data and fits of Equation 2 are shown for solution samples (Samples 1 to 4). The fits to the modeled data from Section 2 are displayed in Figure 3. Figure 4a illustrates that the incoherent scattering signal cannot be described over the entire q-range by a monotonous function (Equation. 2). At low q, the deviation can be explained by the slightly broader resolution function δE, possible coherent scattering contributions or multiple scattering. Thus, we choose to describe S_{inc} by Equation 2 only within $0.5\text{Å}^{-2} < q^2 < 2\text{Å}^{-2}$. Figures 4b-4e show the resulting fits for the different samples.

The extracted $\langle u^2 \rangle_\omega$ is plotted versus $\hbar\omega$ for the different samples investigated in Figure 5. For all solution samples measured, $\langle u^2 \rangle_\omega$ first decays at increasing $\hbar\omega$ before reaching a plateau. Assuming a Fickian diffusion process with a diffusion coefficient D, the energy dependence can be described by[80]

$$\langle u^2 \rangle_\omega = \frac{D}{\delta E}\frac{9\exp\left(\Omega^2\right)}{\pi}\left[1 - 2\Omega F_D(\Omega)\right] \quad (4)$$

with

$$\begin{aligned} F_D(\Omega) &= \exp\left(-\Omega^2\right)\int_0^\Omega \mathrm{d}y \exp\left(y^2\right) \\ &= \frac{1}{2}\sqrt{\pi}\exp\left(-\Omega^2\right)\operatorname{erfi}(\Omega) \quad (5)\end{aligned}$$

and

$$\Omega = \frac{\hbar\omega}{\sqrt{2}\delta E} \quad (6)$$

with $\operatorname{erfi}(x)$ being the imaginary error function. Since at large $\hbar\omega$, the incoherent scattering is dominated by the internal dynamics as discussed in Section 2, deviations from the dependence in Equation 4 are expected at higher $\hbar\omega$ and explain the plateau observed in Figure 5. The dependence of $\langle u^2 \rangle_\omega$ on $\hbar\omega$ is therefore only fitted for lower $\hbar\omega < 1.3$ µeV with

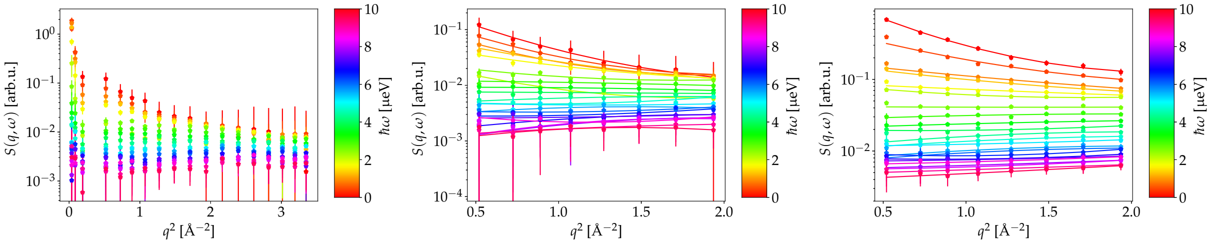

(a) BSA: full q range of Sample 1 (b) BSA: Sample 1 (c) BSA: Sample 2

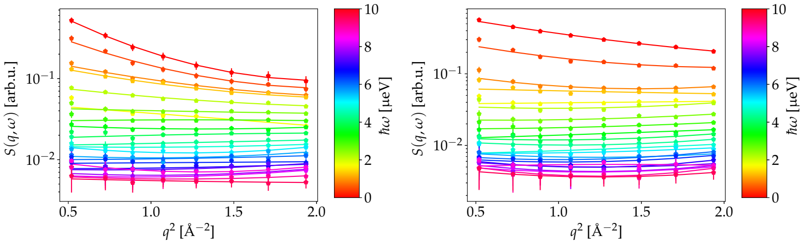

(d) Myo: Sample 3 (e) Ig: Sample 4

Figure 4: Incoherent scattering data (symbols) from protein solutions for different energy transfers $\hbar\omega$ (color-coded) versus the scattering vector q, and fits by Equation 2 (lines). The sample compositions are given in Table 1.

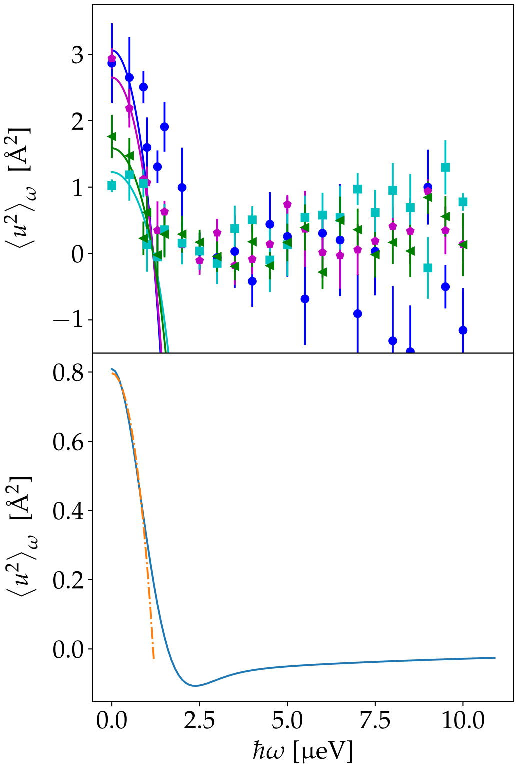

Figure 5: $\langle u^2 \rangle_w$ obtained from the fits shown in Figure 4 versus $\hbar\omega$. Fits of Equation 4 are shown as solid lines. The results are given in Table 3. Top: Experimental results of Samples 1-4 (Table 1) at 280 K. Blue circles, green triangles (◂), magenta pentagons (⬟) and cyan squares represent the values of BSA 100mg/ml and BSA 500mg/ml (Sample 1 and Sample 2), Myo (Sample 3) and IgG (Sample 4), respectively. Bottom: $\langle u^2 \rangle_w$ versus energy transfer for the modeled S_{inc} from Section 2 as blue line. The orange dashed dotted line represents a fit of Equation 4.

Equation 4 by fixing $\delta E = 0.9$ µeV. These fits are shown in Figure 5 and the associated diffusion coefficients in Table 3.

Combining polynomial expressions for the Voigt function[81,82] with a coefficient comparison, a description of the energy dependence of $\langle u^2 \rangle_\omega$ might be possible and allows to investigate further the internal dynamics. However, this approach requires a parametrization of the EISF and of the internal dynamics and will therefore depend on the system. Here we evaluate the parametrized model to evaluate the effect of the internal dynamics (Figure 5, bottom, solid line).

Table 3: Diffusion coefficients obtained from the fits of the energy dependence of $\langle u^2 \rangle_\omega$ at 280 K shown in Figure 5.

#	Sample	D_{GMSD} [Å^2/ns]
1	BSA 100mg/ml	1.46 ± 0.41
2	BSA 500mg/ml	0.76 ± 0.11
3	Myo 500 mg/ml	1.27 ± 0.19
4	polyclonal Ig 500 mg/ml	0.58 ± 0.11
	Modeled data	0.38 ± 0.01

4 Analysis of FWS as Sparse QENS Signals

The previous sections focused on the evaluation of the q-dependence of one single FWS. However, similar to the analysis of full QENS spectra, the collected data can be analyzed by taking both the energy and momentum transfer into account. Moreover, the knowledge and assumptions from the total QENS fits can be used for the data analysis. Several FWS at different $\hbar\omega$ increase the number of independent sampling points. By doing so, either a model free analysis or more complex models accessing more parameters can be used to describe the data. This section will show first approaches of such sparse QENS fits based on FWS, which are recombined to QENS spectra with a very limited number of energy transfers.

To evaluate the FWS, the knowledge obtained from full QENS measurements can be used to construct a fit function. FWS performed sequentially, i.e. kinetically to investigate kinetically changing samples[46,83,84] can be grouped into a sparse QENS spectrum and can then be analyzed similarly to the QENS spectra.

While the polynomial approach to analyze FWS presented in the preceding Section 3 is model-free, the approach presented here relies on modeling existing knowledge from full QENS. On the one hand, based on the Nyquist–Shannon sampling theorem,[85] it can allow to observe faster kinetic changes in the system, *e.g.*, on a timescale of one minute instead of several hours. On the other hand, it might lead to systematic errors if the system changes in a way inconsistent with the model employed. Here, a different number of Voigt functions $\mathscr{V}(\sigma,\gamma)$ is used to describe the experimental data. The parameter σ is fixed based on the resolution function and the scaling parameter as well as γ are kept free as fit parameters.

Depending on the number of fit parameters and the energy transfers available, fits can either be performed similarly to the classical QENS analysis for each momentum transfer separately, or they can be performed for all energy and momentum transfers simultaneously. Fits of the different spectra with one single Voigt function (Figure S7) show a reasonably good agreement for low energy transfers, but larger deviations can be observed at higher energy transfers. To describe the energy dependence more adequately, a second Voigt function is added to the model. The fit results are shown in Figure 6. While most samples show similar fit functions independent on the cutoff ΔE, this agreement clearly depends on the sample dynamics, as expected. It becomes visible that, depending on the hierarchical diffusive processes observable on the time and length scales of the instruments, a different number of energy transfers is necessary to capture all processes. A disentanglement of all contributions is not always straightforward.

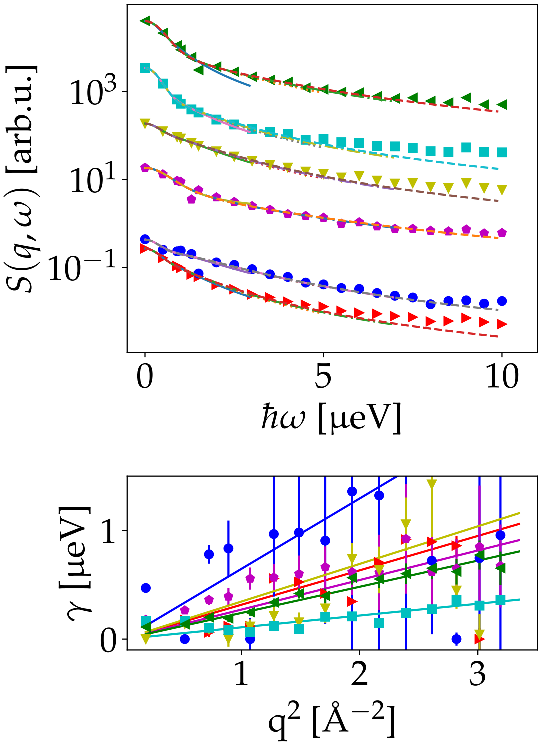

Figure 6: Top: Sparse QENS analysis for different samples using two Voigt functions to fit the energy dependence. A significantly better agreement is observed for high energy transfers, where different diffusive processes contribute substantially to the scattering signal. The fits at $q = 1$ $\mathrm{Å}^{-1}$ for different maximum energy transfers $\hbar\omega_{max} = 3$ μeV (solid blue line), $\hbar\omega_{max} = 5$ μeV (orange dotted line), $\hbar\omega_{max} = 7$ μeV (green dashed dotted line), $\hbar\omega_{max} = 10$ μeV (brown dashed line). The different curves are shifted by factor 10 each for better visibility. Bottom: The q^2-dependence of the corresponding widths of the fit for $\hbar\omega < 10$μeV as well as a fit of $\gamma = Dq^2$ to determine the diffusion coefficient D. In both plots, blue spheres, magenta pentagons, cyan squares, olive down pointing triangles, red right pointing triangles and green left pointing triangles represent values of BSA 100 mg/ml at 280 K, myoglobin 500mg/ml at 280 K, polyclonal IgG 500mg/ml at 280 K, BSA 500 mg/ml at 310 K, BSA 500 mg/ml at 295 K and BSA 500 mg/ml at 280 K, respectively.

5 Extracting Effective Diffusion Coefficients from two FWS at Different Energy Transfers

The most sparse FWS acquisition protocol would be the collection of only two FWS. Here, we address this case by analyzing the FWS in a way motivated by the QENS analysis, but still using a model-free approach. The only assumption within this framework is that the observed broadening of the scattering signal can be described by a Lorentzian function which dominates the scattering signal within the energy trans-

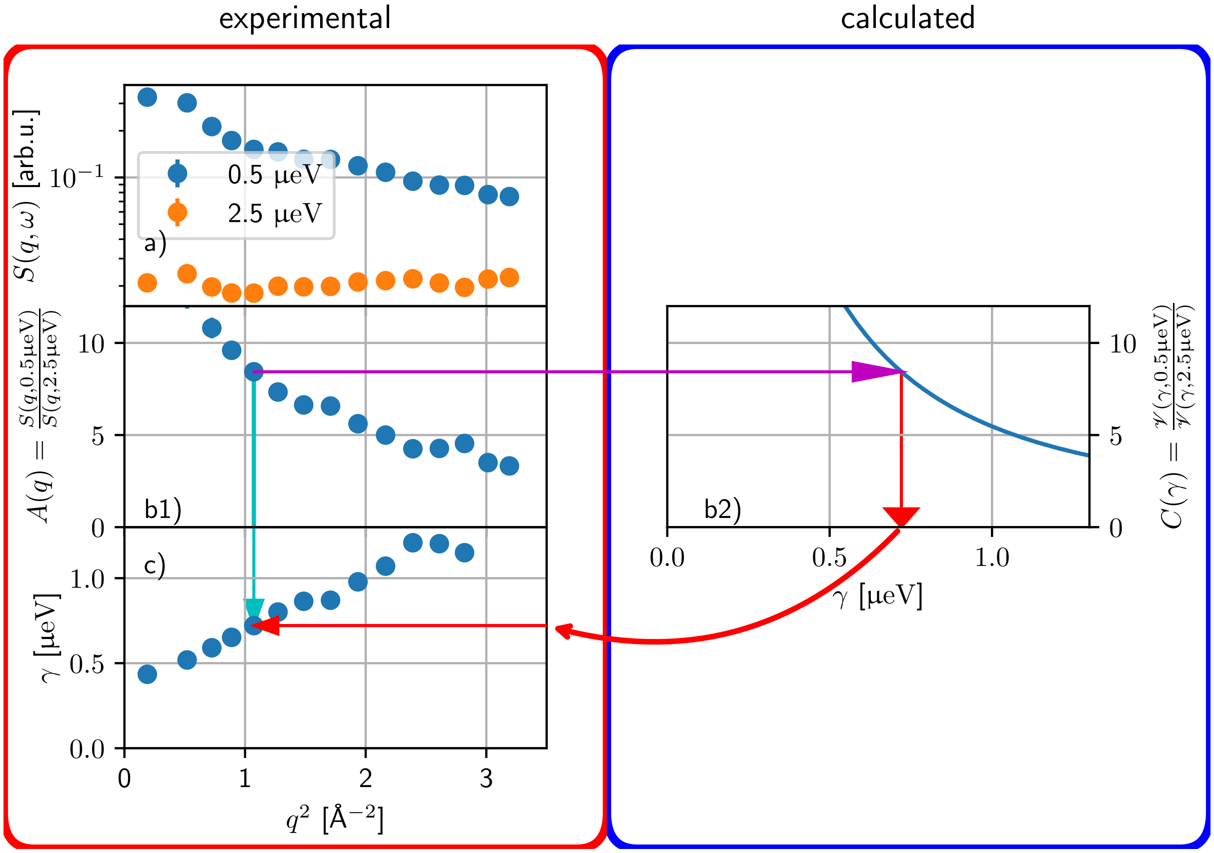

Figure 7: Graphical illustration of the data analysis path explained in Section 5. For illustration, data from polyclonal Ig (Sample 4, Table 1) have been used.

fer investigated. In principle, other line shapes can also be applied. Similar to the analysis of full NBS spectra, this analysis offers a q-dependent HWHM. Several steps, illustrated in Figure 7, are necessary for the analysis:

- For both energy transfers, the empty sample container contribution is subtracted from the FWS. Subsequently, the ratio $A(q) = \frac{S(q,\hbar\omega_i)}{S(q,\hbar\omega_r)}$ between these two FWS is determined (Figure 7 b1).

- To obtain the HWHM as a function of q, a calibration curve $C(\gamma)$ can be calculated (Figure 7 b2).

$$C(\gamma) = \frac{\mathscr{R}_\sigma(\hbar\omega_i) \otimes \mathscr{L}_\gamma(\hbar\omega_i)}{\mathscr{R}_\sigma(\hbar\omega_r) \otimes \mathscr{L}_\gamma(\hbar\omega_r)} \overset{(1)}{=} \frac{\mathscr{V}_{\sigma,\gamma}(\hbar\omega_i)}{\mathscr{V}_{\sigma,\gamma}(\hbar\omega_r)} \qquad (7)$$

with the energy transfers $\hbar\omega_i$ and $\hbar\omega_r$ of both FWS. In step (1), a centered Gaussian function as resolution function is assumed, but more complicated expressions for $\mathscr{R}_\sigma(\hbar\omega)$ are possible in numerical evaluation.

- The calibration curve $C(\gamma)$ is then used to convert the experimental ratio value $A(q)$ into the line broadening $\gamma = C^{-1}(A(q))$ (Figure 7c).

- The q dependence of γ can then be analyzed with known models.

In Figure 8, $C(\gamma)$ is plotted versus γ for different resolutions with FWHM δE. The dependency of $C(\gamma)$ on different energy transfers chosen for the FWS is shown in the SI. The FWHM were chosen to match the resolutions of backscattering spectrometers such as of the GaAs prototype of IN16B ($\delta E = 0.078\,\mu\text{eV}$[86]), of SPHERES ($\delta E = 0.6\,\mu\text{eV}$[87]), of the unpolished Si(111) versions of IN16B,[86] HFBS[15] , and EMU[17] ($\delta E = 0.9\,\mu\text{eV}$), of the IN16B BATS option ($\delta E = 3.5\,\mu\text{eV}$[88–90]), as well as of IN13 ($\delta E = 8\,\mu\text{eV}$[62,63]). In practice, the resolution is not independent from q. Therefore, in general, a q-dependent calibration curve $C(\gamma, q)$ has to be used. This approach has several restrictions concerning the observable global dynamics. If the tracer particle moves too slowly, the ratio observed is dominated by the resolution function and would suggest an immobile particle scattering only elastically. This situation is observed for instance in the case of crystallizing samples.[46] As can be seen in Figure 8, the calibration curves slightly level off at low γ. If an experimental ratio with its corresponding errors close to this value should be translated into the corresponding γ, even a small error in the ratio would lead to a large error in γ.

However, in case of too fast dynamics, the chosen energy offsets do not differ significantly and the ratio is close to unity. Additionally in this case, γ cannot be determined unambiguously anymore. To investigate the influence of the resolution parametrization on the obtained values of γ, the q dependent description of the resolution function of IN16B, using two free Gaussian functions, has been applied, yielding similar results as the analysis using only one single Gaussian function (see Figure S9 in SI).

Looking at $\gamma(q)$, an offset $\gamma(q \to 0) > 0$ can be observed. Therefore, we allow for an offset γ_0 in the fitting and determine D from the q dependence as usual, i.e. we fit the data to

$$\gamma = \gamma_0 + D \cdot q^2. \tag{8}$$

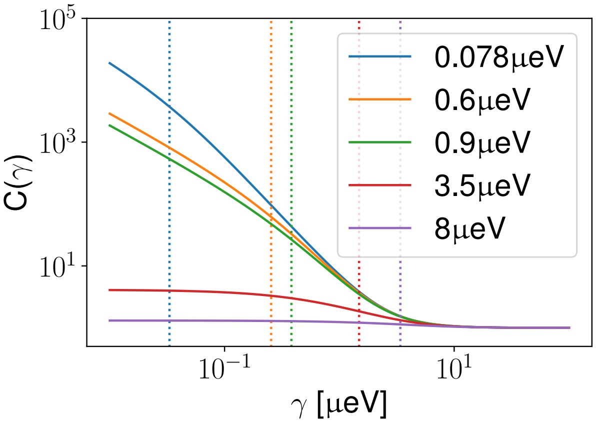

Figure 8: Resolution dependent calibration curves $C(\gamma)$ based on Equation 7 calculated with $\hbar\omega_i = 0$ μeV and $\hbar\omega_r = 2.5$ μeV. Different assumed instrument resolutions are color coded and dashed lines represent the assumed resolution for calculation.

Experimentally, the scattering signal is rarely described by a single diffusive process, since different contributions, such as different hierarchically superimposed diffusive processes and scattering from the solvent are present, which might explain the offset γ_0.

Besides the resolution, also the energy offset of the FWS influences the calibration curve and has to be chosen adequately. When several hierarchical levels of diffusive processes are present, the approximation by a single Lorentzian function may no longer be valid at large $\hbar\omega$. In addition, the solvent becomes more dominant at larger $\hbar\omega$. To ensure that mainly the global dynamics is probed and immobile scatterers do not contribute, one is interested in measuring at small $\hbar\omega > 0$, where the global dynamics dominates the QENS signal. Depending on the system studied, it is therefore important to choose the optimal energy offsets as well as a suitable instrument, which determines the resolution function.

To obtain suitable offsets which result in sample-independent results, we tested systematically different combinations of $\hbar\omega_i$ and $\hbar\omega_r$ on IN16B with Si(111) crystals ($\delta E \approx 0.9$ μeV). In Figure 9, γ is displayed versus q^2 for the different samples in-

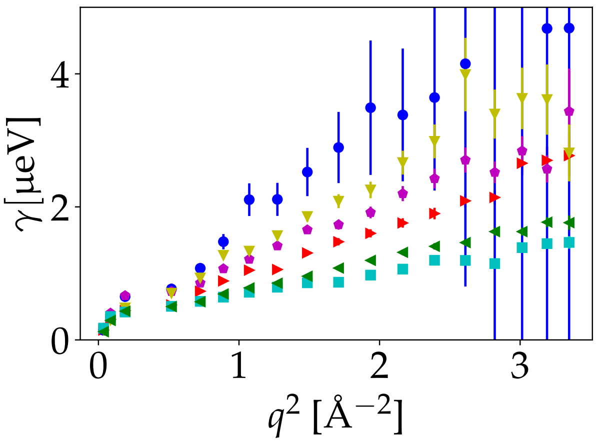

Figure 9: γ versus q^2 derived from FWS collected at $\hbar\omega_i = 0.5$ µeV and $\hbar\omega_r = 2.5$ µeV for the samples investigated. Blue spheres, magenta pentagons, cyan squares, olive down pointing triangles, red right pointing triangles and green left pointing triangles represent values of BSA 100 mg/ml at 280 K, myoglobin 500mg/ml at 280 K, polyclonal IgG 500mg/ml at 280 K, BSA 500 mg/ml at 310 K, BSA 500 mg/ml at 295 K and BSA 500 mg/ml at 280 K, respectively.

vestigated using the energy transfers $\hbar\omega_i = 2.5$ µeV and $\hbar\omega_r = 0.5$ µeV. In Figure 10, the thus obtained diffusion coefficients are plotted versus the diffusion coefficients determined from the full QENS spectra analysis. A reasonable agreement of the two methods is observed with the coefficient of determination $R^2 = 0.97$. In Figure 11, R^2 is displayed for all combinations of energy transfers investigated. It shows that for a good agreement with the results from full QENS spectra, one energy transfer should be below $\hbar\omega \lessapprox 1.5\,\mu\mathrm{eV}$ while the other energy transfer should stay above this threshold. Outside this observed energy transfer range, the q dependence of γ is characterized for many $\hbar\omega$ combinations by a q independent plateau (Figure S8) indicating the limits of the proposed framework.

It should be emphasized that the energy transfers have been found to be reliable for our example protein solutions. For samples with significantly different features in the QENS signal, different optimal

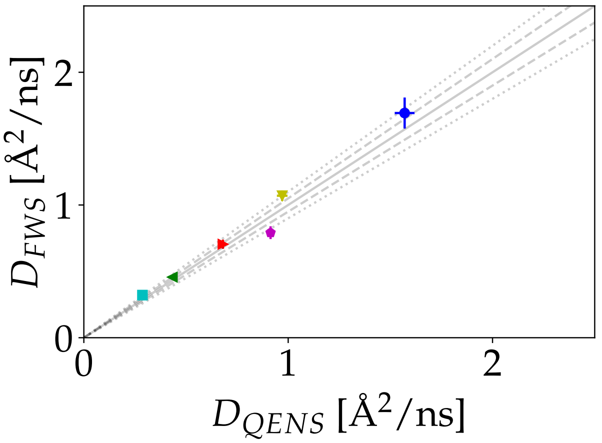

Figure 10: Comparison of the diffusion coefficients obtained from the FWS with those from the full QENS spectra analysis. The different colored symbols represent the samples listed in Table 1. The solid, dashed and dotted lines represent a perfect agreement, as well as a 5% and 10% deviation, respectively.

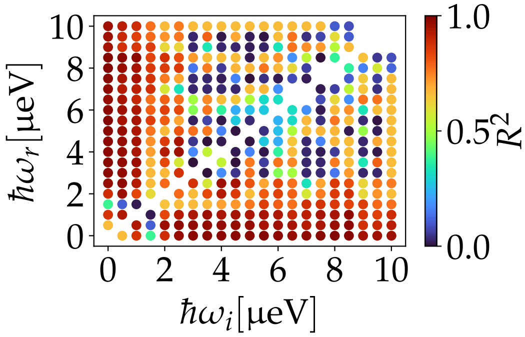

Figure 11: Coefficient of determination of the results obtained from the QENS analysis and the ratio analysis as a function of the chosen energy transfers $\hbar\omega_i$ and $\hbar\omega_r$. A reasonably good agreement can be observed for energy transfers where one of the energy transfers is below and the other above $\hbar\omega = 1.5\,\mu\mathrm{eV}$

energy transfers may apply for their investigation, e.g., mask out the signal of an elastic contribution. Although the choice of the energy transfers may influence the absolute value of the obtained diffusion coefficient D, the method can be applied to qualitatively follow the effect of parameters such as temperature,[27,51] pressure,[91] or time[46,84] on relative changes of D.

6 Applicability to Hydrated Powder Samples

The methods developed above mainly focused on samples in solution. However, the investigation of hydrated powders allows to directly observe the internal diffusive properties of samples by suppressing both the global translational and rotational contribution as well as the contribution from the solvent. The q-dependence of γ can differ from the Fickian diffusion,[92] often present in colloidal suspensions, and can be described by different models[77,93,94] Over the years, different descriptions have been developed and employed for the analysis of EFWS on different hydrated powders.[31,40,43,79,95–100]

The aim of this section is to show the applicability of the methods to powder samples hydrated with H_2O and D_2O, respectively. Different samples have been prepared and measured with different energy transfers as specified in Table 2. It should be emphasized that the change from D_2O to H_2O substantially increases the incoherent contribution of the hydration water. Differences in the obtained results are therefore a combination of possible isotope effects on the system investigated[101] as well as the change in the relative scaling of different contributions.

First, the energy transfers are analyzed in the framework of generalized mean squared displacement. Figures 12 and 13 show the fits by equation 2 as well as the corresponding results for different energy transfers.

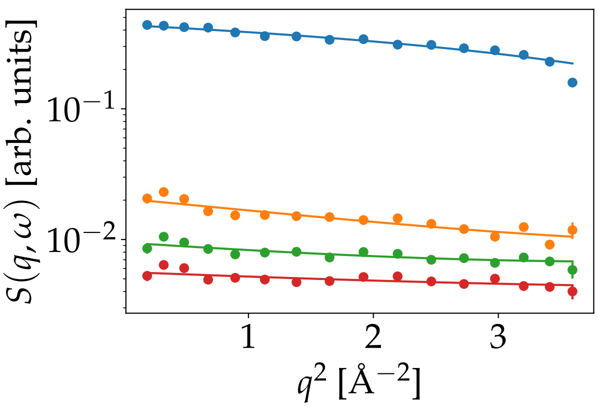

Figure 12: Fits of BSA powder hydrated with H_2O (Sample 5, Table 2) measured on IN16B at T= 280 K using Equation 2. Blue, orange, green and red symbols represent energy transfers of $\hbar\omega = 0$ μeV, $\hbar\omega = 1.3$ μeV, $\hbar\omega = 3$ μeV and $\hbar\omega = 6$ μeV, respectively.

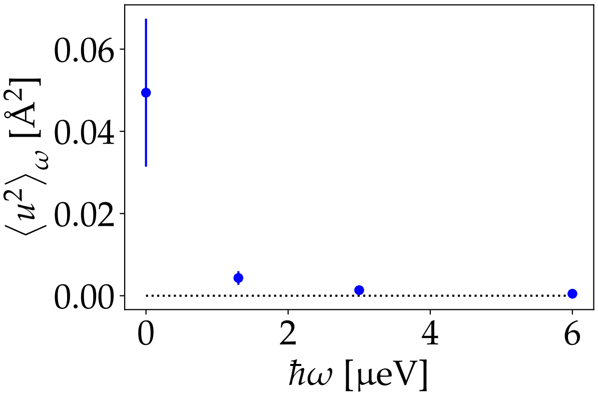

Figure 13: Generalized mean squared displacement of BSA powder hydrated with H_2O (Sample 5) as a function of $\hbar\omega$ obtained from measurements on IN16B (Figure 12) at T=280K.

Since the center of mass motion of the proteins, which has been investigated with the FWS ratios in the solution samples, is not present in the powder samples (i.e., $\gamma = 0$ in Equation 1), the found linewidth corresponds the second Lorentzian Γ in Equation 1. In practical terms, to exclude the elastic peak, two IFWS have to be taken to access Γ from Equation 1. Moreover, the combination of IFWS with EFWS accesses information on the EISF (see SI

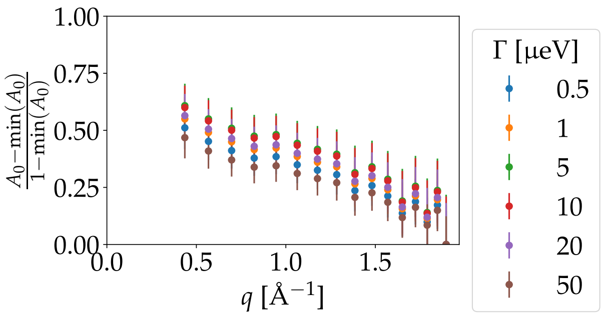

Figure 14: EISF corrected for the immobile fraction determined from FWS recorded from the H_2O hydrated BSA powder. A good agreement can be observed between the results for the different choices of Γ.

Section 7). Based on the energy transfers $\hbar\omega = 3$ µeV and $\hbar\omega = 6$ µeV, we apply the method described in Section 5 to determine $\Gamma(q)$. For the two samples investigated, the q-dependence is shown in FigureS10 for T=280 K. It can be seen that the broadening determined is basically q-independent in the investigated q-range. By investigating the ratio between the EFWS and an IFWS, it is possible to extract the EISF. A detailed procedure is given in the SI. The procedure incorporates the broadening Γ, whose value mainly influences the immobile fraction of the EISF $A_0(q \rightarrow \infty)$. Figure 14 depicts the EISF determined for the H_2O hydrated sample corrected for the immobile fraction for different values of Γ. A good agreement between the curves as well as with the previously obtained EISF of dissolved BSA[27] can be observed.

7 Influence of the Instrument Resolution

To investigate the influence of the instrument resolution on the ratio analysis, the BSA powder samples hydrated with H_2O (Sample 5) and D_2O (Sample 6) were measured on IN13 as a function of temperature with energy transfers $\hbar\omega = 3$ µeV and $\hbar\omega = 9$ µeV. Compared to IN16B, the backscattering spectrometer IN13 is characterized by its higher incident neutron energy,[102] resulting in a broader energy resolution $\delta E \approx 8$µeV but also a significantly larger q range, 0.1 Å^{-1} $< q <$ 4.9 Å^{-1}. A detailed investigation of the influence of the resolution function and the q range has been reported previously.[103]

Assuming that the elastic contribution in the spectra dominates the FWS with the lower energy transfer $\hbar\omega = 3$ µeV, which is nominally within the energy resolution of the instrument, the framework to determine the EISF can be applied. The obtained values also depend on the choice of Γ (see Figure S13). However, a direct renormalization by the immobile fraction as in the case of the EFWS fails. By applying the framework from Section 5, it is possible to determine the broadening Γ. The values for Γ observed on IN13 are comparable to those determined on IN16B with similar offsets ($\hbar\omega_i = 3$ µeV, $\hbar\omega_r = 6$ µeV, see Figure S14). Analogously to the method shown in Section 5, it is therefore possible to determine the internal diffusive properties of the proteins with FWS acquired with energies which are within the energy resolution of the instrument.

8 Conclusions

We have developed a new analysis framework to treat quasi-elastic neutron spectroscopy data recorded at discrete energy transfers and have identified how to optimally choose small sets of energy transfers such that a quantitative agreement can be obtained with the analysis of full QENS spectra. We have demonstrated this framework for a representative range of sample conditions, employing different protein solutions. Moreover, the application of the framework to hydrated powders pointed out the suitability to investigate other systems than suspensions with the same framework. For hydrated powders, the description based on one single Lorentzian function approximating the scattering function in the energy transfer range investigated is not sufficient. Therefore, only relative changes in the obtained parameters (as a function of the solute or temperature) can be investigated. To obtain physically meaningful parameters, the function describing the energy dependence of the scattering function as well as the used energy transfers might have to be adapted.

The concept of fixed-window scans can be generalized. Besides the use of Bragg reflections from crystals, the energy of the incoming neutrons can be defined by the time of flight of pulsed neutron beams, i.e., by the neutron dispersion. The energy resolution of such spectrometers is slightly broader, but significantly higher energy transfers can be accessed (BASIS,[88] IN16B in BATS mode,[89] TOFTOF,[104] MIRACLES,[105] OSIRIS,[106,107] IRIS,[107,108] DNA,[109,110] and MARS[111]). Fixed-window scans are, thus, given by a fixed time of flight window. While the frameworks presented here should be applicable to these scans, the generally larger energy transfers and resolutions will shift the time scales accessed. Moreover, also in neutron spin-echo spectroscopy, the concept of a fixed-window scan may be applied by measuring at a fixed Fourier time while changing a sample parameter such as the temperature.[71,112]

In combination with the available capabilities of neutron backscattering spectrometers at high flux neutron sources, this new framework allows to reduce the acquisition time needed by nearly two orders of magnitude. It can therefore serve to investigate the nanosecond diffusive dynamics in samples that undergo kinetic changes on time scales of minutes, or also the dependencies on control parameters such as pressure, temperature, or light. Thus, topics of current interest including the dynamics of protein aggregation, liquid-liquid phase separation, and crystallization can be investigated. Numerous science cases may be given by systems that evolve on minute time scales. For instance, during a protein crystallization process, the dynamic equilibrium of freely diffusing proteins and of proteins bound to a crystallite may be followed,[46,113] that gradually shift towards the crystalline phase. Light-induced changes on the molecular level in proteins, that are already systematically being investigated by experiments accessing structure,[114] will become accessible to dynamic studies. For instance, in studies of light-induced conformation changes of proteins that are highly relevant for instance in photosynthesis,[115] the gradual relaxation of the protein dynamics to the ground state may be observed. Moreover, the kinetics of pathological protein aggregation may be studied *in vitro*.[84] More generally, the mobility of adsorbates on crystallites, such as organic molecules on ice forming in solution[116,117] may be studied kinetically or at low concentrations, resulting in weak signals. Such adsorption-desorption kinetic phenomena on tiny crystals are important in fields ranging from the food industry[118] to astrophysics,[119] atmospheric chemistry,[120] and even the pipeline industry.[121] In some cases, such as for the said photo-activated proteins, the sample may be reversibly "cycled". Thus, the several offsets for a set of fixed-window data may be recorded consecutively during separate cycles of the identical same sample. In addition, the new framework might improve the scope of neutron sources with lower neutron flux.[122,123] However, we point out that on pulsed neutron sources spectrometers exploiting the time structure of the source – notably via the neutron beam dispersion – to define the incident wavelength are generally preferred over spectrometers with a backscattering monochromator crystal. The fixed window technique, in contrast, achieves its best efficiency on spectrometers equipped with a monochromator crystal to define the incident wavelength.

Further development of the technique may also allow to disentangle distinct diffusive processes by taking more than two energy transfers into account. In this article, we have mainly discussed the moving monochromator setup due to the majority of test experiments performed, but without loss of generality, the concepts are applicable to the temperature-controlled monochromator setup,[20,62,63,86] with the limitation that the temperature change is not quasi-instanteous, or to other designs of switching monochromators, e.g., by a set of monochromators mounted on a disk-type monochromator-changer. Such concepts might be employed for instance at future medium-flux so-called compact neutron sources.[122,123]

9 Data Availability

The neutron data are curated by the ILL and are accessible via References [72–74].

10 Acknowledgements

The authors acknowledge allocation of beamtime at the ILL, the support of the Partnership for Soft Condensed Matter (PSCM), as well as financial support by the DFG and the BMBF (ErUM-pro program / “Verbundforschung”, 05K19VTB and 05K22VTA). We are grateful to Bernhard Frick and Markus Appel for stimulating discussions.

References

[1] A. M. Morris, M. A. Watzky, and R. G. Finke. “Protein aggregation kinetics, mechanism, and curve-fitting: a review of the literature”. *Biochimica et Biophysica Acta (BBA)-Proteins and Proteomics* 1794.3 (2009), pp. 375–397.

[2] G. Meisl et al. “Molecular mechanisms of protein aggregation from global fitting of kinetic models”. *Nature Protocols* 11.2 (2016), pp. 252–272.

[3] X. Sun, H. J. Dyson, and P. E. Wright. “Kinetic analysis of the multistep aggregation pathway of human transthyretin”. *Proceedings of the National Academy of Sciences* 115.27 (2018), E6201–E6208.

[4] Z. Toprakcioglu et al. “Label-free analysis of protein aggregation and phase behavior”. *ACS Nano* 13.12 (2019), pp. 13940–13948.

[5] J. E. Bramham and A. P. Golovanov. “Temporal and spatial characterisation of protein liquid-liquid phase separation using NMR spectroscopy”. *Nature Communications* 13.1 (2022), p. 1767.

[6] J. A. Housmans et al. “A guide to studying protein aggregation”. *The FEBS Journal* 290.3 (2023), pp. 554–583.

[7] X. Sun, H. J. Dyson, and P. E. Wright. “Role of conformational dynamics in pathogenic protein aggregation”. *Current Opinion in Chemical Biology* 73 (2023), p. 102280.

[8] J. T. Jarrett and P. T. Lansbury Jr. “Seeding “one-dimensional crystallization” of amyloid: a pathogenic mechanism in Alzheimer’s disease and scrapie?” *Cell* 73.6 (1993), pp. 1055–1058.

[9] S. I. Cohen et al. “From macroscopic measurements to microscopic mechanisms of protein aggregation”. *Journal of Molecular Biology* 421.2-3 (2012), pp. 160–171.

[10] P. Arosio et al. “Chemical kinetics for drug discovery to combat protein aggregation diseases”. *Trends in Pharmacological Sciences* 35.3 (2014), pp. 127–135.

[11] M. Grimaldo et al. “Dynamics of Proteins in Solution”. *Q. Rev. Biophys.* 52 (2019), e7.

[12] A. Girelli et al. “Microscopic Dynamics of Liquid-Liquid Phase Separation and Domain Coarsening in a Protein Solution Revealed by X-Ray Photon Correlation Spectroscopy”. *Phys. Rev. Lett.* 126.13 (2021).

[13] L. van Hove. “Correlations in Space and Time and Born Approximation Scattering in Systems of Interacting Particles”. *Phys. Rev.* 95.1 (1954), pp. 249–262.

[14] B. Frick and M. Gonzalez. “Five years operation of the second generation backscattering spectrometer IN16—a retrospective, recent developments and plans”. *Physica B: Condens. Matter* 301.1-2 (2001), pp. 8–19.

[15] A. Meyer et al. “The high-flux backscattering spectrometer at the NIST Center for Neutron Research”. *Rev. Sci. Instrum.* 74.5 (Apr. 2003), pp. 2759–2777.

[16] B. Frick et al. “Recent Backscattering Instrument Developments at the ILL and SNS”. *Z. Phys. Chem.* 224.1-2 (2010), pp. 33–60.

[17] N. R. de Souza, A. Klapproth, and G. N. Iles. “EMU: High-Resolution Backscattering Spectrometer at ANSTO”. *Neutron News* 27.2 (2016), pp. 20–21.

[18] M. Zamponi and M. Khaneft. “SPHERES: Backscattering spectrometer”. *JLSRF* 1 (Aug. 2015).

[19] M. Hennig. "Dynamics of Globular Proteins in Crowded Electrolyte Solutions". PhD thesis. Eberhard Karls University Tuebingen, 2011.

[20] J. Cook et al. "A dynamic range upgrade for neutron backscattering spectroscopy". *NIM-A* 312.3 (1992), pp. 553–560.

[21] L Ciampolini et al. "A new gradient monochromator for the IN13 back-scattering spectrometer". *NIM-A* 544.3 (2005), pp. 649–658.

[22] M. T. F. Telling. *A Practical Guide to Quasi-elastic Neutron Scattering*. The Royal Society of Chemistry, July 2020.

[23] M. Kruteva. "Dynamics studied by Quasielastic Neutron Scattering (QENS)". *Adsorption* 27.5 (Feb. 2021), pp. 875–889.

[24] J. Peters et al. "Effects of Crowding and Cosolutes on Biomolecular Function at Extreme Environmental Conditions". *Chemical Reviews* 123.23 (2023), pp. 13441–13488.

[25] S. Zheng et al. "Colossal electrocaloric effect in an interface-augmented ferroelectric polymer". *Science* 382.6674 (2023), pp. 1020–1026.

[26] W. Zhao et al. "Proteome-wide 3D structure prediction provides insights into the ancestral metabolism of ancient archaea and bacteria". *Nature Communications* 13.1 (Dec. 2022).

[27] M. Grimaldo et al. "Hierarchical Molecular Dynamics of Bovine Serum Albumin in Concentrated Aqueous Solution Below and Above Thermal Denaturation". *Phys. Chem. Chem. Phys.* 17 (6 2015), pp. 4645–4655.

[28] W. Doster and M. Settles. "Protein–water displacement distributions". *Biochimica et Biophysica Acta (BBA) - Proteins and Proteomics* 1749.2 (2005). Solvent Effects, pp. 173–186.

[29] W. Doster and S. Longeville. " Microscopic Diffusion and Hydrodynamic Interactions of Hemoglobin in Red Blood Cells". *Biophys. J.* 93.4 (2007), pp. 1360 –1368.

[30] W. Doster. "The dynamical transition of proteins, concepts and misconceptions". *Eur. Biophys. J.* 37 (5 2008), pp. 591–602.

[31] D. Zeller et al. "Analysis of elastic incoherent neutron scattering data beyond the Gaussian approximation". *J. Chem. Phys.* 149.23 (2018), p. 234908.

[32] G. Zaccai. "Neutron scattering perspectives for protein dynamics". *Journal of Non-Crystalline Solids* 357.2 (2011). 6th International Discussion Meeting on Relaxation in Complex Systems, pp. 615–621.

[33] G. R. Kneller. "Franck–Condon picture of incoherent neutron scattering". *Proceedings of the National Academy of Sciences* 115.38 (Aug. 2018), pp. 9450–9455.

[34] G. R. Kneller. "Inelastic neutron scattering from damped collective vibrations of macromolecules". *Chemical Physics* 261.1–2 (Nov. 2000), pp. 1–24.

[35] R. Zorn. "On the evaluation of neutron scattering elastic scan data". *Nuclear Instruments and Methods in Physics Research Section A: Accelerators, Spectrometers, Detectors and Associated Equipment* 603.3 (May 2009), pp. 439–445.

[36] G. H. Vineyard. "Scattering of Slow Neutrons by a Liquid". *Phys. Rev.* 110.5 (1958), p. 999.

[37] C. Caronna, F. Natali, and A. Cupane. " Incoherent Elastic and Quasi-Elastic Neutron Scattering Investigation of Hemoglobin Dynamics". *Biophys. Chem.* 116.3 (2005), pp. 219–225.

[38] S. König et al. "Molecular dynamics of lipid bilayers studied by incoherent quasi-elastic neutron scattering". *Journal de Physique II* 2.8 (Aug. 1992), pp. 1589–1615.

[39] G. Zaccai. "How Soft Is a Protein? A Protein Dynamics Force Constant Measured by Neutron Scattering". *Science* 288.5471 (June 2000), pp. 1604–1607.

[40] W. Doster, S. Cusack, and W. Petry. “Dynamical transition of myoglobin revealed by inelastic neutron scattering”. *Nature* 337.6209 (Feb. 1989), pp. 754–756.

[41] G. Zaccai et al. “Incoherent elastic neutron scattering as a function of temperature : A fast way to characterise in-situ biological dynamics in complex solutions”. *Le Journal de Physique IV* 10.PR7 (May 2000), Pr7–283–Pr7–287.

[42] W Doster, H Nakagawa, and M. Appavou. “Scaling analysis of bio-molecular dynamics derived from elastic incoherent neutron scattering experiments”. *The Journal of Chemical Physics* 139.4 (2013).

[43] Z. Yi et al. “ Derivation of Mean-Square Displacements for Protein Dynamics from Elastic Incoherent Neutron Scattering”. *J. Phys. Chem. B* 116.16 (2012), pp. 5028–5036.

[44] S. Magazù et al. “Mean square displacement evaluation by elastic neutron scattering self-distribution function”. *Physical Review E* 77.6 (June 2008).

[45] G. Eckold, H. Schober, and S. E. Nagler, eds. *Studying Kinetics with Neutrons.* Springer Berlin Heidelberg, 2010.

[46] C. Beck et al. “ Following Protein Dynamics in Real-Time During Crystallization”. *Cryst. Growth Des.* 19.12 (2019), pp. 7036–7045.

[47] M. Busch et al. “Ionic liquid dynamics in nanoporous carbon: A pore-size- and temperature-dependent neutron spectroscopy study on supercapacitor materials”. *Physical Review Materials* 4.5 (May 2020).

[48] R. Guégan et al. “Molecular dynamics of a short-range ordered smectic phase nanoconfined in porous silicon”. *The Journal of Chemical Physics* 126.6 (Feb. 2007).

[49] B. Frick et al. “The nanosecond proton dynamics of phosphoric acid – from the solid to the melt – investigated by neutron backscattering”. *Solid State Ionics* 252 (Dec. 2013), pp. 26–33.

[50] D. Noferini et al. “Proton jump diffusion dynamics in hydrated barium zirconates studied by high-resolution neutron backscattering spectroscopy”. *Journal of Materials Chemistry A* 6.17 (2018), pp. 7538–7546.

[51] O. Matsarskaia et al. “Evolution of the structure and dynamics of bovine serum albumin induced by thermal denaturation”. *Phys. Chem. Chem. Phys.* 22.33 (2020), pp. 18507–18517.

[52] D. Di Bari et al. “Diffusive Dynamics of Bacterial Proteome as a Proxy of Cell Death”. *ACS Cent. Sci.* 9.1 (2023), pp. 93–102.

[53] S. R. Al-Ayoubi et al. “Osmolytes modify protein dynamics and function of tetrameric lactate dehydrogenase upon pressurization”. *Phys. Chem. Chem. Phys.* 21.24 (2019), pp. 12806–12817.

[54] A. M. Stadler et al. “Photoactivation Reduces Side-Chain Dynamics of a LOV Photoreceptor”. *Biophys. J.* 110.5 (2016), pp. 1064 –1074.

[55] A. M. Stadler et al. “Ternary Complex Formation and Photoactivation of a Photoenzyme Results in Altered Protein Dynamics”. *J. Phys. Chem. B* 123.34 (2019), pp. 7372–7384.

[56] M. Grimaldo et al. “ Salt-Induced Universal Slowing Down of the Short-Time Self-Diffusion of a Globular Protein in Aqueous Solution”. *J. Phys. Chem. Lett.* 6.13 (2015), pp. 2577–2582.

[57] M. Appel and B. Frick. “ Note: One Order of Magnitude Better Signal-to-Noise Ratio for Neutron Backscattering”. *Rev. Sci. Instrum.* 88.3 (2017), p. 036105.

[58] H. Bordallo et al. “ Primary Spectrometer Neutron Optics Simulations for a new Cold Neutron Backscattering Spectrometer”. *J. Neutron Res.* 16.1-2 (2008), pp. 39–54.

[59] J. Schelten and B. Alefeld. *Proc. Workshop on Neutron Scattering: Instrumentation for SNQ, Report Ml 1954 (KFA Jülich, 1984).* 1984.

[60] M. Hennig, B. Frick, and T. Seydel. "Optimum Velocity of a Phase-Space Transformer for Cold-Neutron Backscattering Spectroscopy". *J. Appl. Crystallogr.* 44.3 (2011), pp. 467–472.

[61] J. Pieper et al. "Transient Protein Softening during the Working Cycle of a Molecular Machine". *Phys. Rev. Lett.* 100 (22 2008), p. 228103.

[62] F Natali et al. " IN13 Backscattering Spectrometer: An Instrument in Evolution". *Phys. B* 350.1, Supplement (2004), E819 –E822.

[63] F. Natali et al. "IN13 Backscattering Spectrometer at ILL: Looking for Motions in Biological Macromolecules and Organisms". *Neutron News* 19.4 (Nov. 2008), pp. 14–18.

[64] B. Frick. " Neutron and X-ray Spectroscopy: Neutron Backscattering Spectroscopy". Ed. by F. Hippert et al. Dordrecht: Springer Netherlands, 2006, pp. 483–527.

[65] B. Frick et al. " How IN16 can Maintain a World-Leading Position in Neutron Backscattering Spectrometry". *Phys. B (Amsterdam, Neth.)* 385-386 (2006), pp. 1101 –1103.

[66] B. Frick, J. Combet, and L. van Eijck. "New possibilities with inelastic fixed window scans and linear motor Doppler drives on high resolution neutron backscattering spectrometers". *Z. Phys. Chem.* 669 (2012), pp. 7–13.

[67] B Frick et al. "Study of the glass transition order parameter in amorphous polybutadiene by incoherent neutron scattering". *Zeitschrift für Physik B Condensed Matter* 70 (1988), pp. 73–79.

[68] M. Grimaldo et al. " Diffusion and Dynamics of γ- Globulin in Crowded Aqueous Solutions". *J. Phys. Chem. B* 118 (2014), pp. 7203–7209.

[69] F. Roosen-Runge et al. "Protein self-diffusion in crowded solutions". *Proc. Natl. Acad. Sci. USA* 108.29 (2011), pp. 11815–11820.

[70] M. Grimaldo et al. "Protein Short-Time Diffusion in a Naturally Crowded Environment". *J. Phys. Chem. Lett.* 10.8 (2019), pp. 1709–1715.

[71] A. Girelli et al. "Molecular Flexibility of Antibodies Preserved Even in the Dense Phase after Macroscopic Phase Separation". *Molecular Pharmaceutics* 18.11 (Oct. 2021), pp. 4162–4169.

[72] C. Beck et al. *Developing new analysis methods for fixed window scans for soft colloidal suspensions.* Institut Laue-Langevin (ILL); doi:10.5291/ILL-DATA.1-20-69. 2021.

[73] C. Beck et al. *Studying thermal protein denaturation as a nanoscopic structure-dynamics relationship.* Institut Laue-Langevin (ILL) doi:10.5291/ILL-DATA.9-13-637. 2016.

[74] M. Grimaldo et al. *Monitoring anomalous diffusion and dynamical arrest using elastic and inelastic fixed window scans at neutron backscattering.* Institut Laue-Langevin (ILL) doi:10.5291/ILL-DATA.9-13-628. 2016.

[75] M. Grimaldo et al. "High-resolution neutron spectroscopy on protein solution samples". *EPJ Web of Conf.* 83 (2015), p. 02005.

[76] M. Bee. *Quasielastic Neutron Scattering: Principles and Applications in Solid State Chemistry, Biology and Material Science.* Adam Hilger, Bristol, 1988.

[77] K. Singwi and A. Sjölander. " Diffusive Motions in Water and Cold Neutron Scattering". *Phys. Rev.* 119.3 (1960), pp. 863–871.

[78] A. Rahman, K. S. Singwi, and A. Sjölander. "Theory of Slow Neutron Scattering by Liquids. I". *Phys. Rev.* 126.3 (May 1962), pp. 986–996.

[79] T. Becker and J. C. Smith. "Energy resolution and dynamical heterogeneity effects on elastic incoherent neutron scattering from molecular systems". *Phys. Rev. E* 67.2 (Feb. 2003).

[80] F. Roosen-Runge and T. Seydel. “ A generalized mean-squared displacement from inelastic fixed window scans of incoherent neutron scattering as a model-free indicator of anomalous diffusion confinement”. *EPJ Web of Conf.* 83 (2015), p. 02015.

[81] A. N. Hassani, A. M. Stadler, and G. R. Kneller. “Quasi-analytical resolution-correction of elastic neutron scattering from proteins”. *J. Chem. Phys.* 157.13 (Oct. 2022).

[82] M. Saouessi, J. Peters, and G. R. Kneller. “Frequency domain modeling of quasielastic neutron scattering from hydrated protein powders: Application to free and inhibited human acetylcholinesterase”. *J. Chem. Phys.* 151.12 (Sept. 2019).

[83] K. Pounot et al. “High-resolution Neutron Spectroscopy to Study Picosecond-nanosecond Dynamics of Proteins and Hydration Water”. *JoVE* 182 (2022), e63664.

[84] K. Pounot et al. “Tracking Internal and Global Diffusive Dynamics During Protein Aggregation by High-Resolution Neutron Spectroscopy”. *J. Phys. Chem. Lett.* 11.15 (July 2020), pp. 6299–6304.

[85] C. Shannon. “Communication In The Presence Of Noise”. *Proc. IEEE* 86.2 (Feb. 1998), pp. 447–457.

[86] K. Kuhlmann et al. “ Breakthrough in Neutron Backscattering Spectroscopy: Energy Resolution Improved by One Order of Magnitude Using the GaAs 200 Reflection”. *Rev. Sci. Instrum.* 90.1 (2019), p. 015119.

[87] J. Wuttke et al. “SPHERES, Jülich-s high-flux neutron backscattering spectrometer at FRM II”. *Rev. Sci. Instrum.* 83.7 (July 2012), p. 075109.

[88] E. Mamontov and K. W. Herwig. “ A Time-of-Flight Backscattering Spectrometer at the Spallation Neutron Source, BASIS”. *Rev. Sci. Instrum.* 82.8 (2011), p. 085109.

[89] M. Appel, B. Frick, and A. Magerl. “A flexible high speed pulse chopper system for an inverted neutron time-of-flight option on backscattering spectrometers”. *Sci. Rep.* 8.1 (Sept. 2018).

[90] C. Beck et al. “ Neutron Spectroscopy on Protein Solutions Employing Backscattering with an Increased Energy Range”. *Phys. B (Amsterdam, Neth.)* 562 (2019), pp. 31–35.

[91] A. Caliò et al. “Unravelling the Adaptation Mechanisms to High Pressure in Proteins”. *Int. J. Mol. Sci.* 23.15 (2022).

[92] A. Fick. “Ueber Diffusion”. *Ann. Phys.* 170.1 (1855), pp. 59–86.

[93] C. T. Chudley and R. J. Elliott. “Neutron Scattering from a Liquid on a Jump Diffusion Model”. *Proc. Phys. Soc.* 77.2 (1961), p. 353.

[94] P. L. Hall and D. Ross. “Incoherent neutron scattering functions for random jump diffusion in bounded and infinite media”. *Mol. Phys.* 42.3 (Feb. 1981), pp. 673–682.

[95] G. R. Kneller and G. Chevrot. “ Impact of Anisotropic Atomic Motions in Proteins on Powder-Averaged Incoherent Neutron Scattering Intensities”. *Chem. Phys.* 137.22 (2012), p. 225101.

[96] A. Tokuhisa et al. “Non-Gaussian behavior of elastic incoherent neutron scattering profiles of proteins studied by molecular dynamics simulation”. *Physical Review E* 75.4 (Apr. 2007).

[97] J. Peters and G. R. Kneller. “Motional heterogeneity in human acetylcholinesterase revealed by a non-Gaussian model for elastic incoherent neutron scattering”. *The Journal of Chemical Physics* 139.16 (Oct. 2013), p. 165102.

[98] D. Vural et al. “ Motional Displacements in Proteins: The Origin of Wave-Vector-Dependent Values”. *Phys. Rev. E* 91 (5 2015), p. 052705.

[99] Z. Liu et al. “Dynamical Transition of Collective Motions in Dry Proteins”. *Phys. Rev. Lett.* 119 (4 2017), p. 048101.

[100] T. Matsuo and J. Peters. “Sub-Nanosecond Dynamics of Pathologically Relevant Bio-Macromolecules Observed by Incoherent Neutron Scattering”. *Life* 12.8 (Aug. 2022), p. 1259.

[101] M. K. Braun et al. “ Strong Isotope Effects on Effective Interactions and Phase Behavior in Protein Solutions in the Presence of Multivalent Ions”. *J. Phys. Chem. B* 121.7 (2017), pp. 1731–1739.

[102] S. Teixeira et al. “New sources and instrumentation for neutrons in biology”. *Chem. Phys.* 345.2-3 (Apr. 2008), pp. 133–151.

[103] F. Gabel. “Protein dynamics in solution and powder measured by incoherent elastic neutron scattering: the influence of Q-range and energy resolution”. *European Biophysics Journal* 34.1 (Sept. 2004), pp. 1–12.

[104] T. Unruh, J. Neuhaus, and W. Petry. “The high-resolution time-of-flight spectrometer TOFTOF”. *Nuclear Instruments and Methods in Physics Research Section A: Accelerators, Spectrometers, Detectors and Associated Equipment* 580.3 (Oct. 2007), pp. 1414–1422.

[105] N. Tsapatsaris et al. “ Conceptual Design of the Time-of-Flight Backscattering Spectrometer, MIRACLES, at the European Spallation Source”. *Rev. Sci. Instrum.* 87.8 (2016), p. 085118.

[106] M. T. F. Telling and K. H. Andersen. “Spectroscopic characteristics of the OSIRIS near-backscattering crystal analyser spectrometer on the ISIS pulsed neutron source”. *Phys. Chem. Chem. Phys.* 7.6 (2005), pp. 1255–1261.

[107] F. Demmel et al. “ToF-Backscattering spectroscopy at the ISIS Facility: Status and Perspectives”. *Journal of Physics: Conference Series* 1021 (May 2018), p. 012027.

[108] S. Campbell, M. Telling, and C. Carlile. “The optimisation of analyser geometry in near-backscattering spectrometers – IRIS on the ISIS-pulsed source”. *Physica B: Condensed Matter* 276–278 (Mar. 2000), pp. 206–207.

[109] K. Shibata et al. “The Performance of TOF near Backscattering Spectrometer DNA in MLF, J-PARC”. *Proceedings of the 2nd International Symposium on Science at J-PARC — Unlocking the Mysteries of Life, Matter and the Universe —*. Journal of the Physical Society of Japan, Sept. 2015.

[110] H. Seto et al. “Inelastic and quasi-elastic neutron scattering spectrometers in J-PARC”. *Biochimica et Biophysica Acta (BBA) - General Subjects* 1861.1 (Jan. 2017), pp. 3651–3660.

[111] P. Tregenna-Piggott, F. Juranyi, and P. Allenspach. “Introducing the inverted-geometry time-of-flight backscattering instrument, MARS at SINQ”. *Journal of Neutron Research* 16.1 (Mar. 2008), pp. 1–12.

[112] J Kulda et al. “Self-energy of zone-boundary phonons in germanium: Ab initio calculations versus neutron spin-echo measurements”. *Physical review B* 69.4 (2004), p. 045209.

[113] A. Sauter et al. “Real-Time Observation of Nonclassical Protein Crystallization Kinetics”. *J. Am. Chem. Soc.* 137.4 (2015), pp. 1485–1491.

[114] K. Röllen et al. “Small-angle X-ray scattering study of the kinetics of light-dark transition in a LOV protein”. *PLoS One* 13.7 (2018), e0200746.

[115] M. Golub et al. “Light-Induced Conformational Flexibility of the Orange Carotenoid Protein Studied by Quasielastic Neutron Scattering with In Situ Illumination”. *The journal of physical chemistry letters* 14.1 (2023), pp. 295–301.

[116] S. Clarke and T Arnold. “Simultaneous coherent and incoherent neutron scattering of polyalcohols adsorbed on ice”. *Applied Physics A* 74 (2002), s1371–s1372.

[117] J. Joliat et al. “Adsorption of C2–C5 alcohols on ice: A grand canonical Monte Carlo simulation study”. *The Journal of Chemical Physics* 156.22 (2022).

[118] G. Petzold and J. M. Aguilera. “Ice morphology: fundamentals and technological applications in foods”. *Food Biophysics* 4 (2009), pp. 378–396.

[119] A. A. Boogert, P. A. Gerakines, and D. C. Whittet. “Observations of the icy universe”. *Annual Review of Astronomy and Astrophysics* 53 (2015), pp. 541–581.

[120] S. Solomon. “Stratospheric ozone depletion: A review of concepts and history”. *Reviews of geophysics* 37.3 (1999), pp. 275–316.

[121] D. Kashchiev and A. Firoozabadi. “Induction time in crystallization of gas hydrates”. *Journal of crystal growth* 250.3-4 (2003), pp. 499–515.

[122] F. Ott et al. “ICONE – Towards a French HiCANS Neutron Source for materials science and industry”. *EPJ Web of Conf.* 286 (2023). Ed. by I. Lommatzsch et al., p. 02001.

[123] T. Brückel et al. “The High Brilliance neutron Source (HBS): A project for a next generation neutron research facility”. *EPJ Web of Conf.* 286 (2023). Ed. by I. Lommatzsch et al., p. 02003.